

A multimodal Transformer for InSAR-based ground deformation forecasting with cross-site generalization across Europe

Wendong Yao^{a,b}, Binhua Huang^{a,b}, Soumyabrata Dev^{a,b,*}

^a*The ADAPT SFI Research Centre, Dublin, Ireland*

^b*School of Computer Science, University College Dublin, Belfield, Dublin, Ireland*

Abstract

Near-real-time regional-scale monitoring of ground deformation is increasingly required to support urban planning, critical infrastructure management, and natural hazard mitigation. While Interferometric Synthetic Aperture Radar (InSAR) and continental-scale services such as the European Ground Motion Service (EGMS) provide dense observations of past motion, predicting the next observation remains challenging due to the superposition of long-term trends, seasonal cycles, and occasional abrupt discontinuities (e.g., co-seismic steps), together with strong spatial heterogeneity.

In this study we propose a multimodal patch-based Transformer for single-step, fixed-interval next-epoch nowcasting of displacement maps from EGMS time series (resampled to a 64×64 grid over $100 \text{ km} \times 100 \text{ km}$ tiles). The model ingests recent displacement snapshots together with (i) static kinematic indicators (mean velocity, acceleration, seasonal amplitude) computed in a leakage-safe manner from the training window only, and (ii) harmonic day-of-year encodings. On the eastern Ireland tile (E32N34), the STGCN is strongest in the displacement-only setting, whereas the multimodal Transformer clearly outperforms CNN-LSTM, CNN-LSTM+Attn, and multimodal STGCN when all models receive the same multimodal inputs, achieving RMSE = 0.90 mm and $R^2 = 0.97$ on the test set with the best threshold accuracies.

We further assess transferability by training a single model on E32N34 and applying it, without fine-tuning, to five unseen European tiles spanning continuous subsidence, periodic motion, and co-seismic deformation. Across all six tiles the model maintains $R^2 \geq 0.93$, with RMSE ranging from 0.7 to 3.2 mm and 71–87% of pixels within 1 mm. For co-seismic tiles, the high overall accuracy reflects robustness to strong time-series discontinuities and rapid post-event re-alignment once the step is present in the input history, rather than anticipation of earthquake occurrence. These results indicate that multimodal Transformers can serve as accurate local nowcasters and transferable priors for EGMS-based deformation monitoring with limited local training data.

Keywords: Interferometric Synthetic Aperture Radar (InSAR), Land subsidence Prediction, Multimodal deep learning, Cross-site generalisation

1. Introduction

Ground deformation driven by groundwater extraction, underground construction, hydrocarbon production and tectonic processes poses a persistent threat to buildings, transportation networks and critical infrastructure worldwide [1, 2, 3, 4]. Interferometric Synthetic Aperture Radar (InSAR) has become a key technology for mapping such deformation with millimetre accuracy over large areas [5, 6, 7], and continental-scale services such as the European Ground Motion Service (EGMS) now deliver harmonised ground-motion products across Europe [8, 9]. However, these products are intrinsically retrospective: they describe how the ground has moved so far, but not how it is likely to move at the next acquisitions. In many operational settings, even short-term information at the cadence of new satellite passes (on the order of a few days for Sentinel-

1 over Europe) can help operators track the evolution of deformation signals and prioritise sites for further investigation, complementing more traditional geodetic and engineering assessments rather than replacing them.

Within Europe, these capabilities have recently been consolidated in the European Ground Motion Service (EGMS), an operational Copernicus Land Monitoring Service product based on Sentinel-1 SAR data [8, 9]. EGMS delivers homogenised, quality-controlled ground motion information over the European continent, including line-of-sight displacement time series and summary statistics such as mean velocity, linear acceleration and seasonal-motion parameters on a regular grid. This open and systematic service removes the need for bespoke InSAR processing for many applications and offers, for the first time, continental-scale time series of ground motion suitable for statistical analysis and machine-learning modelling [10].

Most current uses of EGMS and other InSAR products remain retrospective: they focus on mapping and attribution of observed deformation, for example by identifying subsiding urban districts, unstable slopes or regions of aquifer compaction [11, 12]. Only a limited number of studies have attempted to

*Corresponding author. Tel.: + 353 1896 1797.

Email addresses: wendong.yao@ucdconnect.ie (Wendong Yao), binhua.huang@ucdconnect.ie (Binhua Huang), soumyabrata.dev@ucd.ie (Soumyabrata Dev)

forecast future ground motion using data-driven models, despite the potential value of short-term predictive capability for monitoring and maintenance workflows [13]. Recent work has begun to explore deep learning approaches for InSAR time series, for instance using convolutional and recurrent neural networks to detect deformation patterns or to model local displacement histories at specific sites [13]. However, these applications are typically restricted to one or a few locations, treat each pixel independently, or rely on relatively simple network architectures.

Spatio-temporal deep learning models designed for structured data provide a natural way to exploit both the temporal dynamics and spatial correlation of InSAR ground-motion fields. Spatio-temporal graph convolutional networks (STGCNs) [14], originally developed for traffic forecasting, combine temporal convolutions with graph convolutions defined on a fixed adjacency structure and have proven effective for learning complex propagation patterns in networked systems. Self-attention and Transformer architectures, first proposed for natural language processing, have subsequently been adapted for time-series forecasting and for modelling spatial-temporal processes, allowing models to learn long-range and non-local dependencies without an explicit graph.

At the same time, most existing forecasting studies in ground deformation still adopt a uni-modal perspective, using only the displacement time series as input [13]. In contrast, operational products such as EGMS expose a richer set of information [9]: in addition to per-epoch displacement, each grid cell is associated with static motion descriptors (e.g. mean velocity, linear acceleration, seasonal amplitude) summarising its long-term behaviour, and the acquisition dates themselves encode clear seasonal cycles. Incorporating this multi-modal information into spatio-temporal deep learning models has the potential to improve forecasting skill, but this opportunity has not yet been systematically explored.

In our previous work we proposed a convolutional neural network-long short-term memory (CNN-LSTM) architecture for short-term InSAR ground deformation forecasting over eastern Ireland, using only sequences of displacement maps as input [15]. While this uni-modal approach achieved promising skill, particularly when combined with an STGCN baseline on the same grid, its accuracy remained limited in regions with strong seasonal variability or low signal-to-noise ratio, and it did not explicitly exploit the static descriptors already available from the EGMS processing chain.

Also, this manuscript is related to our earlier study on EGMS/InSAR deformation forecasting [16], which investigated window-based forecasting models that are primarily trained and evaluated in a site-specific manner. In contrast, the focus here is on *transferable* single-step forecasting: we introduce a multimodal formulation that leverages EGMS-derived static deformation indicators and harmonic time encodings, and we develop a patch-based Transformer that is evaluated under cross-site regimes, including zero-shot transfer across multiple European tiles. Accordingly, the model design choices, experimental protocols (cross-site and leakage-safe feature construction), and conclusions differ from [16].

The present study addresses these gaps by moving from a uni-modal to a multi-modal representation of EGMS ground motion and by systematically evaluating both graph-based and attention-based spatio-temporal deep learning architectures. We construct a unified grid-based data set for a 100 km \times 100 km EGMS tile covering eastern Ireland, in which each sample consists of: (i) a sequence of displacement maps; (ii) three static ground-motion indicator maps derived from the EGMS Level 3 product (mean velocity, acceleration and seasonal amplitude); and (iii) sinusoidal encodings of the acquisition day-of-year. On this multi-modal input we train and compare four architectures: a convolutional–recurrent CNN–LSTM, its attention-augmented variant, a multi-modal STGCN and a newly designed spatio-temporal Transformer that operates on multi-channel image patches with global self-attention and residual next-step prediction.

In this work we focus on *single-step, fixed-interval* forecasting at the native EGMS/Sentinel-1 cadence, i.e. predicting the displacement map at the next available acquisition given a history of past observations and auxiliary variables. Such next-epoch forecasts are best viewed as a form of deformation *nowcasting* and short-term trend projection, intended to support routine monitoring, screening and infrastructure management rather than stand-alone, long-horizon early-warning systems.

Our main contributions are threefold:

- We construct a multimodal learning framework that combines recent displacement maps with static auxiliary layers and temporal encodings, enabling the model to jointly exploit spatial susceptibility, seasonal forcing and local deformation history. We show that this multimodal design substantially improves single-step prediction accuracy over using displacement maps alone.
- We design a dedicated Transformer architecture tailored to InSAR-based deformation forecasting and benchmark it against convolutional sequence models (CNN–LSTM, CNN–LSTM with attention) and a state-of-the-art spatio-temporal graph convolutional network (STGCN). On a tile in eastern Ireland, the proposed multimodal Transformer achieves the best overall single-step performance across RMSE, MAE, R^2 and multiple error-threshold accuracies.
- Beyond local experiments, we systematically evaluate the spatial transferability of the multimodal Transformer. A model trained only on a single EGMS tile (E32N34) generalises well to five additional tiles representing continuous subsidence, periodic motion, co-seismic displacement and quasi-stable conditions, maintaining $R^2 \geq 0.93$ and high sub-millimetre accuracy. This demonstrates the potential of Transformer-based models as transferable priors for large-scale, EGMS-driven deformation nowcasting in regions with limited local training data.

2. Data and study areas

2.1. European Ground Motion Service data

Our analysis is based on the Level 3 (L3) products of the European Ground Motion Service (EGMS), part of the Copernicus Land Monitoring Service. EGMS provides harmonized ground-motion information over the European continent derived from multi-temporal interferometric processing of Sentinel-1 SAR images [8, 9]. The L3 product is a regularly gridded data set in which each grid cell aggregates one or more persistent or distributed scatterers and stores a displacement time series along with several summary statistics and quality indicators. For each grid cell, the L3 Up component used in this study contains:

- the time series of vertical displacement with respect to a reference epoch;
- the mean velocity estimated from a linear trend fit to the time series;
- a linear acceleration term capturing long-term curvature;
- parameters describing the amplitude and phase of annual seasonal motion, derived from harmonic regression; and
- various uncertainty and quality metrics, including the standard deviation of residuals.

The underlying Sentinel-1 constellation provides a revisit time of 6 days over Europe in the ascending and descending orbits, enabling dense temporal sampling of ground motion at a nominal spatial resolution of approximately 20–30 m. The EGMS processing chain applies consistent orbit corrections, atmospheric delay mitigation, geocoding and rigorous quality control, producing a homogeneous long-term record of surface deformation suitable for regional and continental-scale applications. In this work we exploit this consistency to study both local forecasting skill and cross-site generalization of our multimodal Transformer across different deformation regimes in Europe.

For each 100 km × 100 km tile, the L3 Up product is delivered as a comma-separated values (CSV) file named EGMS_L3_EXXNYY_100km_U_2018_2022_1.csv, where EXXNYY encodes the tile identifier in the EGMS tiling grid. The file contains all grid cells in the tile, with columns storing the geographic coordinates, ground-motion summary statistics and a series of displacement values for each Sentinel-1 acquisition between 2018 and 2022. We focus on this recent 5-year period to align with the operational EGMS version and to avoid potential artefacts associated with the transition from the Sentinel-1A-only to the Sentinel-1A/B constellation.

2.2. Study areas and deformation regimes

To evaluate both local performance and cross-site generalization, we select six EGMS tiles distributed across Europe, chosen to represent a broad spectrum of ground-motion behaviours. Tiles are identified using the standard EGMS naming convention, **EXXNYY**, where:

- **XX** denotes the easting coordinate (in 100 km units, EPSG:3035) of the south-west corner of the tile’s lower-left pixel; and

- **YY** denotes the corresponding northing coordinate.

The six tiles are grouped into three categories according to their dominant deformation regime:

- **Continuous and periodic deformation:** Tiles E32N34 and E32N35 are located on the east coast of Ireland and encompass the greater Dublin region and surrounding low-lying coastal plain. Previous work has shown that these tiles exhibit a rich mixture of slow subsidence bowls, localized uplift and pronounced seasonal signals related to hydrogeological forcing and anthropogenic loading. Tile E32N34 serves as our primary *source* tile for training the multimodal Transformer, while both E32N34 and E32N35 are used to assess forecasting skill in regions dominated by gradual, often quasi-periodic deformation.
- **Long-term subsidence:** Tiles E39N30 and E44N23 provide examples of more monotonic, long-term subsidence. These tiles cover urban and industrial areas underlain by compressible sediments and engineering structures where subsidence is driven by natural consolidation, groundwater extraction and surface loading. They are used to test whether a model trained on mixed-periodic behaviour can extrapolate persistent downward trends in previously unseen settings.
- **Abrupt co-seismic displacement:** Tiles E48N24 and E58N17 encompass regions that experienced strong co-seismic deformation during recent moderate-to-large earthquakes. These data are characterized by sharp spatial gradients and step-like temporal offsets superimposed on otherwise relatively stable background motion. They constitute the most challenging scenario for cross-site generalization, probing the ability of the model to reproduce sudden structural breaks in the time series.

Across all tiles, the EGMS L3 product provides a dense sampling of ground motion over built-up areas, transport corridors, exposed rock and other coherent scatterers. As is typical for C-band SAR, coverage is sparser in vegetated and agricultural zones, but the gridded product retains sufficient density to enable interpolation to a regular raster representation suitable for convolutional and Transformer-based neural networks.

2.3. Pre-processing and feature construction

To build a common input representation for all models and tiles, we convert the irregular grid of EGMS L3 points into a stack of raster maps at a spatial resolution of 64×64 pixels covering the full 100 km × 100 km extent of each tile. For every acquisition epoch, the vertical displacement values are interpolated onto this grid using linear scattered-data interpolation in the projected (easting, northing) coordinate system, yielding a displacement cube of size $T \times H \times W$ per tile.

We then define a chronological training window covering the first 80 % of available epochs ($t = 1, \dots, T_{\text{train}}$) and a test window comprising the remaining 20 % ($t = T_{\text{train}} + 1, \dots, T$). All static deformation indicators used in this work are *recomputed* from the training window only, in order to avoid leakage of information from future epochs. Concretely, for each grid cell we fit a simple polynomial-plus-harmonic model to the training portion of the time series and derive (i) a mean velocity, (ii) a quadratic acceleration term and (iii) the amplitude of the dominant annual component. These three statistics are then interpolated onto the same 64×64 grid to form time-invariant “static” maps per tile. We do not use the EGMS L3 summary parameters that are fitted over the full 2018–2022 time series.

For a given tile, the resulting data cube has dimensions $T \times C \times H \times W$, where T is the number of acquisition epochs (about 300 in our case), $H = W = 64$, and C denotes the number of input channels. For the uni-modal setting we use only the displacement channel ($C = 1$). For the multimodal setting we construct a six-channel representation ($C = 6$) consisting of:

1. the displacement map at each epoch;
2. three static maps encoding mean velocity, acceleration and seasonal amplitude, all estimated from the training window only;
3. two temporal encoding channels given by the sine and cosine of the normalised day-of-year of the acquisition date, which capture the annual cycle in a smooth, periodic form.

Before model training, all channels are standardised. Static channels are normalised per-channel using their spatial mean and standard deviation. Displacement time series are standardised on a per-pixel basis using statistics computed from the training portion of the corresponding tile, and the same affine transformation is then applied to all time steps of that tile. This prevents information leakage from the test window into the training process while preserving the relative amplitudes of seasonal and long-term motions.

Finally, we construct supervised learning samples by sliding a temporal window of length T_{in} over the normalised displacement cube. For each window, the input consists of T_{in} consecutive multi-channel maps, and the target is the displacement map at the next time step. In this paper we focus on single-step forecasting with $T_{\text{in}} = 16$ for the Transformer and a comparable historical context for the other models. Sequence pairs are split in chronological order into a training set (first 80 % of samples) and a validation/test set (remaining 20 %), ensuring that all models are evaluated on strictly unseen future data. For the cross-site generalisation experiments, the network is trained only on tile E32N34 using its training window, and then applied, without fine-tuning, to the test windows of the remaining tiles using the same input representation and normalisation strategy.

2.3.1. Resolution sensitivity analysis

In this work we deliberately operate at a regional grid resolution of 64×64 pixels over each $100 \text{ km} \times 100 \text{ km}$ tile, corresponding to a pixel spacing of approximately 1.56 km. This

Table 1: Resolution sensitivity for a CNN–LSTM baseline on tile E32N34 (displacement-only, SmoothL1 loss). Metrics are computed on the last 20 % of epochs.

Resolution	RMSE [mm]	MAE [mm]	R^2	Acc@1mm [%]
64×64	1.96	1.16	0.87	60.02
128×128	1.79	1.11	0.88	60.78

choice reflects a trade-off between spatial detail and the memory requirements of training multimodal 3D spatio-temporal networks on several hundred Sentinel-1 epochs. Increasing the grid to 128×128 or 256×256 would lead to a $4\times$ or $16\times$ increase in the number of spatial degrees of freedom per time step, which is prohibitive for the multimodal Transformer under our GPU budget.

Rather than targeting infrastructure-scale motion at the level of individual buildings, we focus here on regional-scale forecasting of ground deformation on a $\sim 1.5 \text{ km}$ grid, which is directly compatible with tile-wise EGMS products and suitable for city- and basin-scale risk screening.

To address the potential influence of spatial downsampling on forecast skill, we conducted a small-scale sensitivity experiment on tile E32N34. In the main experiments, all models operate on rasterised EGMS L3 inputs resampled to a 64×64 grid (Section 2), corresponding to a pixel spacing of approximately 1.5 km. Here we retrain a lighter CNN–LSTM baseline, using the same displacement-only configuration and training protocol as in Section 4, but at two different spatial resolutions: 64×64 and 128×128 .

Table 1 summarises the results on the last 20 % of the time series for both settings. Increasing the resolution from 64×64 to 128×128 yields a modest reduction in RMSE from 1.96 mm to 1.79 mm and a slight increase in R^2 from 0.87 to 0.88. Threshold accuracies are essentially unchanged: Acc@1mm improves only from 60.0 % to 60.8 %, and the tighter thresholds (0.5, 0.2 and 0.1 mm) differ by less than 0.5 percentage points.

These findings indicate that, for the EGMS L3 products and deformation patterns considered in this study, doubling the grid resolution does not lead to substantial gains in single-step forecast performance. The 64×64 representation therefore appears sufficient to capture the dominant spatial structure of the displacement field, while providing a favourable trade-off between fidelity and computational efficiency for training the more demanding multimodal Transformer and STGCN models.

3. Methodology

3.1. Problem formulation

Let $\Omega \subset \mathbb{R}^2$ denote the spatial domain of an EGMS tile, discretised on a regular $H \times W$ grid, and let $t \in \{1, \dots, T\}$ index the Sentinel-1 acquisition epochs. For each grid cell $(i, j) \in \{1, \dots, H\} \times \{1, \dots, W\}$ and time t , the EGMS L3 Up product provides a vertical displacement $d_t(i, j)$ in millimetres with respect to a reference epoch (Section 2).

We cast short-term ground deformation forecasting as a supervised spatio-temporal learning task. Given a sequence of L

historical displacement maps

$$\mathbf{D}_{t-L+1:t} = \{d_\tau(i, j) \mid \tau = t - L + 1, \dots, t; (i, j) \in \Omega\}, \quad (1)$$

together with time-invariant descriptors $\mathbf{S}(i, j)$ of the local deformation regime and explicit temporal encodings \mathbf{h}_τ of acquisition date, the goal is to predict the displacement field at the next epoch,

$$\hat{d}_{t+1}(i, j) = f_\theta(\mathbf{D}_{t-L+1:t}, \mathbf{S}, \mathbf{h}_{t-L+1:t+1}), \quad (2)$$

where f_θ is a deep neural network with learnable parameters θ . Throughout this work we focus on single-step forecasting ($t+1$), but the formulation naturally extends to multi-step horizons.

As detailed in Section 2, we construct supervised samples by sliding a fixed-length temporal window of size $L = T_{\text{in}}$ along each EGMS time series. Each window yields an input tensor $\mathbf{X}_n \in \mathbb{R}^{L \times C \times H \times W}$ and a corresponding target $\mathbf{Y}_n \in \mathbb{R}^{1 \times 1 \times H \times W}$, where C is the number of input channels after fusing all modalities. We adopt a chronological 80/20 split in the temporal dimension: the first 80% of epochs are used for training and the remaining 20% for validation and testing, thereby avoiding information leakage from future acquisitions.

Figure 1 shows overall workflow of our proposed EGMS-based multimodal deformation nowcasting framework.

3.2. Multimodal input representation

3.2.1. Displacement-only representation

In our previous work [15] we modelled EGMS ground motion using displacement maps only. Each input sample consisted of a sequence of L vertical displacement fields,

$$\mathbf{X}_n^{\text{disp}} \in \mathbb{R}^{L \times 1 \times H \times W}, \quad (3)$$

and the network was tasked with predicting the next displacement map. This single-modality setting provides a strong baseline and demonstrates that deep spatio-temporal models can already capture long-term subsidence trends and seasonal deformation patterns in EGMS data.

3.2.2. Multimodal spatio-temporal representation

To more explicitly expose physically meaningful factors that influence ground deformation, we extend the input representation to three complementary modalities, consistent with the feature construction described in Section 2:

1. **Dynamic displacement history.** The first modality is the normalised sequence of EGMS displacement maps $\mathbf{D}_{t-L+1:t}$, identical to the uni-modal setting.
2. **Static deformation indicators.** From the *training portion* of the EGMS time series at each grid cell we derive three summary statistics that characterise its long-term behaviour: (i) mean velocity, (ii) linear acceleration, and (iii) the amplitude of the dominant seasonal component. These indicators form a static feature tensor

$$\mathbf{S} \in \mathbb{R}^{3 \times H \times W}, \quad (4)$$

which is broadcast along the temporal dimension so that each time step receives the same spatially varying static context. Importantly, we recompute these indicators using only the training window for each tile, rather than using the EGMS L3 parameters fitted over the full 2018–2022 series, to avoid any leakage of information from test epochs into the predictors.

3. **Temporal encodings.** To inject information about acquisition date and seasonality directly into the model, we encode the day-of-year of each epoch τ using a harmonic representation,

$$\mathbf{h}_\tau = [\sin(2\pi\tau/T_{\text{year}}), \cos(2\pi\tau/T_{\text{year}})], \quad (5)$$

where $T_{\text{year}} \approx 365.25$. The resulting two time features are tiled across the spatial grid, yielding a tensor of shape $2 \times H \times W$ per time step. This encoding allows the networks to learn seasonally dependent dynamics in a translation-invariant manner, as is common in time-series transformers and temporal convolutional models.

Stacking all three modalities along the channel dimension leads to a unified multimodal input of shape

$$\mathbf{X}_n \in \mathbb{R}^{L \times C \times H \times W}, \quad (6)$$

$$C = 1 \text{ (displacement)} + 3 \text{ (static)} + 2 \text{ (time)} = 6.$$

3.2.3. Normalisation

To stabilise optimisation and ensure comparability across space and time, we apply modality-specific normalisation.

Displacement. For experiments where a model is trained and evaluated on a single tile, we compute a per-pixel mean and standard deviation using only the training portion of the time series,

$$\mu_d(i, j) = \frac{1}{T_{\text{train}}} \sum_{t=1}^{T_{\text{train}}} d_t(i, j),$$

$$\sigma_d(i, j) = \sqrt{\frac{1}{T_{\text{train}}} \sum_{t=1}^{T_{\text{train}}} (d_t(i, j) - \mu_d(i, j))^2 + \varepsilon}. \quad (7)$$

and normalise as $d_t^{\text{norm}}(i, j) = (d_t(i, j) - \mu_d(i, j)) / \sigma_d(i, j)$, with ε preventing division by zero. For cross-site experiments, the statistics $\mu_d(i, j)$ and $\sigma_d(i, j)$ are estimated on the source tile (E32N34) and applied unchanged to the input displacement maps of the target tiles, so that the model sees test-time input distributions scaled in the same way as during training.

Static indicators. For the static features we use channel-wise normalisation, subtracting the spatial mean and dividing by the spatial standard deviation over all pixels of each indicator. In all cases, these statistics are computed from the static maps derived on the training window, and the resulting affine transform is then applied to the static channels for the full time series.

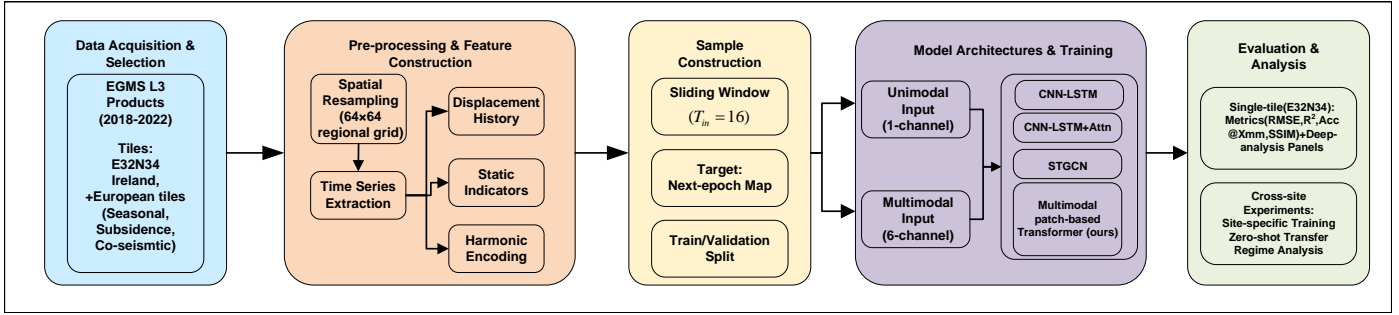


Figure 1: Overall workflow of the proposed EGMS-based multimodal deformation nowcasting framework, from EGMS L3 data acquisition through pre-processing and sample construction to model training and single-tile / cross-site evaluation.

Temporal encodings. The sinusoidal encodings are naturally bounded in $[-1, 1]$ and are used without additional scaling.

At inference time, model predictions in normalised units are transformed back to millimetres using the inverse of the per-pixel displacement normalisation, enabling direct comparison with EGMS products and geophysical thresholds.

3.3. Model architectures

We benchmark four families of spatio-temporal neural networks that are representative of the main design paradigms used in geoscientific forecasting: a convolutional recurrent baseline (CNN-LSTM), an attention-augmented variant, a spatio-temporal graph convolutional network (STGCN), and the proposed multimodal transformer.

3.3.1. CNN-LSTM baseline

The first baseline is a convolutional neural network followed by a long short-term memory (CNN-LSTM) network, a widely used architecture for modelling spatio-temporal sequences such as precipitation nowcasting and traffic flow [e.g. 17]. For each time step, a stack of 2-D convolutions with ReLU activations and spatial pooling encodes the C -channel input map into a compact latent representation:

$$\mathbf{z}_\tau = g_\phi(\mathbf{X}_n[\tau]) \in \mathbb{R}^F, \quad \tau = t - L + 1, \dots, t, \quad (8)$$

where g_ϕ denotes the convolutional encoder and F is the flattened feature dimension. The resulting sequence $(\mathbf{z}_{t-L+1}, \dots, \mathbf{z}_t)$ is passed to a bidirectional LSTM, which captures temporal dependencies and outputs a sequence of hidden states $\mathbf{h}_\tau \in \mathbb{R}^{H_{\text{LSTM}}}$. We aggregate temporal information by summing the hidden states and feed the resulting context vector into a deconvolutional decoder composed of fully connected and transposed convolution layers. This decoder upsamples the latent representation back to the original spatial resolution, producing the predicted map $\hat{d}_{t+1}(i, j)$.

3.3.2. Attention-augmented CNN-LSTM

To explicitly model the varying importance of different past epochs, we construct an attention-augmented variant of the CNN-LSTM. After obtaining the sequence of LSTM hidden

states \mathbf{h}_τ , we compute a scalar attention score e_τ for each time step via a shallow multilayer perceptron:

$$e_\tau = \mathbf{w}^\top \tanh(\mathbf{W}_a \mathbf{h}_\tau + \mathbf{b}_a), \quad (9)$$

normalise the scores with a softmax over time to obtain weights α_τ , and form a context vector as the weighted sum

$$\mathbf{c} = \sum_{\tau=t-L+1}^t \alpha_\tau \mathbf{h}_\tau. \quad (10)$$

This context vector is then decoded to the output map using the same deconvolutional decoder as in the baseline. The attention mechanism allows the network to focus on epochs that are most informative for the impending deformation, for instance strong seasonal peaks or recent transients, which is particularly relevant for ground-motion analysis.

3.3.3. Multimodal STGCN

Graph-based methods offer an alternative view on spatio-temporal dynamics by representing the study area as a graph and learning on its nodes. We adopt a multimodal variant of the spatio-temporal graph convolutional network (STGCN) originally proposed for traffic forecasting [14].

Each grid cell (i, j) is treated as a node, and we construct an undirected graph by connecting each node to its eight spatial neighbours (queen adjacency), plus a self-loop. From this adjacency matrix \mathbf{A} we compute the symmetric normalised matrix $\tilde{\mathbf{A}} = \mathbf{D}^{-1/2}(\mathbf{A} + \mathbf{I})\mathbf{D}^{-1/2}$, where \mathbf{D} is the degree matrix. The input tensor is rearranged to shape $[B, C, N, L]$, where $N = H \times W$ is the number of nodes and B is the batch size.

An STGCN block consists of a temporal gated convolution, a graph convolution, and a second temporal convolution. The temporal unit applies 1-D convolutions along the time dimension with a gated linear unit (GLU) non-linearity:

$$\mathbf{X}' = \sigma(\mathbf{W}_{\text{in}} * \mathbf{X}) \odot (\mathbf{W}_{\text{out}} * \mathbf{X}), \quad (11)$$

where $*$ denotes convolution over time, σ is the sigmoid function, and \odot is the element-wise product. Graph convolution is then performed as

$$\mathbf{X}'' = \mathbf{W}_g \mathbf{X}' \tilde{\mathbf{A}}, \quad (12)$$

where \mathbf{W}_g is a learnable weight matrix. A residual connection and layer normalisation stabilise training. Stacking two such

blocks yields a tensor of shape $[B, C', N, L]$, which is reshaped to $[B, N, C'L]$ and passed through a fully connected layer to predict the displacement at $t + 1$ for each node. The node-wise predictions are finally reshaped back to the image grid.

All modalities (displacement history, static indicators, temporal encodings) are concatenated along the channel axis at the network input. This enables the STGCN to exploit both local graph structure and cross-modal interactions when propagating information over time. We refer to this configuration as MM-STGCN in the experiments.

3.3.4. Multimodal spatio-temporal transformer (ours)

Our main contribution is a multimodal spatio-temporal transformer tailored to dense ground-deformation forecasting. The design is inspired by the success of transformer architectures in sequence modelling and vision tasks [18], but adapted to handle EGMS displacement cubes in an efficient, patch-based manner. Figure 2 shows the architecture of the Conceptual model.

Patch embedding and tokenisation... Each input tensor $\mathbf{X}_n \in \mathbb{R}^{L \times C \times H \times W}$ is partitioned into non-overlapping spatial patches of size $P \times P$. For each time step and patch we flatten the $C \times P \times P$ values into a vector and map it to a D -dimensional embedding using a linear projection (with layer normalisation). This yields a sequence of $L \times N_p$ tokens $\mathbf{z}_{1:(LN_p)} \in \mathbb{R}^D$, where $N_p = (H/P) \times (W/P)$ is the number of patches.

Temporal query tokens... Instead of autoregressively unrolling the transformer over time, we append a set of learnable query tokens that correspond to the future time steps we wish to predict (here $t + 1$). The final input sequence to the transformer encoder is

$$\mathbf{Z}_0 = [\mathbf{z}_{1:(LN_p)}, \mathbf{q}_{1:(L_{\text{out}}N_p)}] + \mathbf{P}, \quad (13)$$

where \mathbf{q} denotes the query embeddings, $L_{\text{out}} = 1$ for single-step prediction, and \mathbf{P} is a learnable positional encoding that encodes both temporal index and patch location.

Masked self-attention... We employ a standard multi-head self-attention encoder with K layers. In each layer, tokens are first normalised and then projected to queries, keys and values, followed by scaled dot-product attention and a feed-forward network:

$$\text{Attn}(\mathbf{Q}, \mathbf{K}, \mathbf{V}) = \text{softmax}\left(\frac{\mathbf{Q}\mathbf{K}^T}{\sqrt{d_k}} + \mathbf{M}\right)\mathbf{V}, \quad (14)$$

$$\mathbf{Z}_{t+1} = \mathbf{Z}_t + \text{Attn}_t(\mathbf{Z}_t) + \text{FFN}_t(\mathbf{Z}_t), \quad (15)$$

where \mathbf{M} is an additive attention mask. To preserve causality, we mask attention from historical tokens to query tokens, while allowing the queries to attend to all tokens in the sequence. This design lets the future representations integrate information from all past patches and modalities, while preventing leakage of predicted information back into the encoder.

Patch decoding and residual prediction.... After the final layer we extract the subset of tokens corresponding to the future query positions and project each D -dimensional embedding back to $C_{\text{out}}P^2$ pixels via a linear decoder and layer normalisation. The resulting patch-wise predictions are rearranged to form a displacement increment map $\tilde{d}_{t+1}(i, j)$. We adopt a residual formulation in which the model predicts a correction to the last observed displacement,

$$\hat{d}_{t+1}(i, j) = d_t(i, j) + \tilde{d}_{t+1}(i, j), \quad (16)$$

which empirically stabilises training and focuses the network on modelling short-term increments rather than absolute displacements.

3.4. Training objectives and optimisation

All models are trained to minimise a combination of pixel-wise reconstruction losses and structural regularisers that encourage physically plausible deformation patterns. Let $\hat{\mathbf{Y}}_n$ be the predicted normalised displacement map and \mathbf{Y}_n the corresponding ground truth for sample n .

Reconstruction losses.... Our primary objective is the mean absolute error (MAE) computed in normalised units,

$$\mathcal{L}_{\text{MAE}} = \frac{1}{B} \sum_{n=1}^B \|\hat{\mathbf{Y}}_n - \mathbf{Y}_n\|_1, \quad (17)$$

where B is the mini-batch size. To better reflect relative discrepancies in millimetres, we also consider a relative error term computed after de-normalisation:

$$\mathcal{L}_{\text{rel}} = \frac{1}{B} \sum_{n=1}^B \frac{\|\hat{\mathbf{Y}}_n^{\text{mm}} - \mathbf{Y}_n^{\text{mm}}\|_1}{\|\mathbf{Y}_n^{\text{mm}}\|_1 + \varepsilon}, \quad (18)$$

where \mathbf{Y}_n^{mm} denotes the de-normalised map in physical units.

Correlation and gradient regularisation.... To promote coherence between predicted and observed spatial patterns, we add two regularisers for the transformer model. First, we penalise 1 minus the Pearson correlation coefficient between the flattened prediction and ground truth for each sample. Second, we introduce a gradient loss that measures the MAE between Sobel-filtered horizontal and vertical gradients of $\hat{\mathbf{Y}}_n^{\text{mm}}$ and \mathbf{Y}_n^{mm} . This term encourages sharper subsidence bowls and preserves local discontinuities, which are important for interpreting deformation signals near infrastructure and faults.

Overall objective and optimisation.... The overall loss is given by

$$\mathcal{L} = \mathcal{L}_{\text{MAE}} + \lambda_{\text{rel}} \mathcal{L}_{\text{rel}} + \lambda_{\text{corr}} \mathcal{L}_{\text{corr}} + \lambda_{\text{grad}} \mathcal{L}_{\text{grad}}, \quad (19)$$

where the weighting factors λ are tuned on the validation set. For the CNN-LSTM baselines and the STGCN we primarily use \mathcal{L}_{MAE} (i.e. $\lambda_{\text{rel}} = \lambda_{\text{corr}} = \lambda_{\text{grad}} = 0$), matching conventional practice in related work, while for the transformer we exploit the full composite objective to maximise structural fidelity.

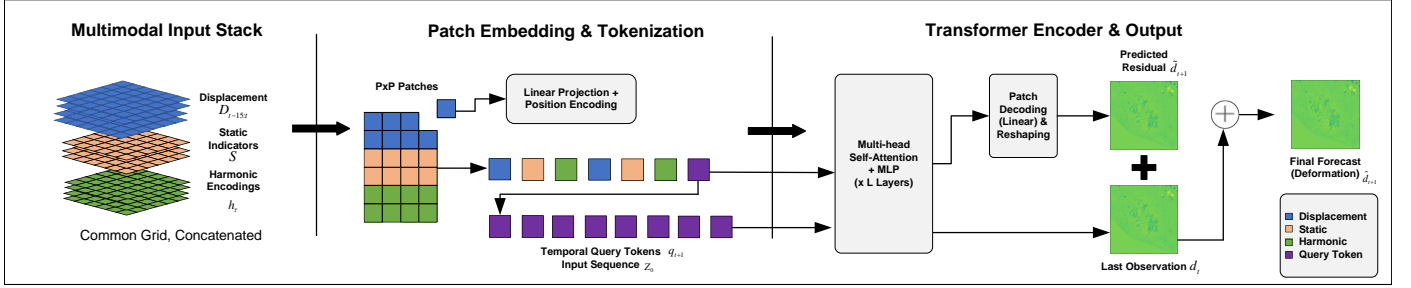


Figure 2: Conceptual architecture of the multimodal patch-based Transformer for EGMS ground-motion forecasting. For each tile and acquisition epoch, the vertical displacement history, static deformation indicators, and harmonic day-of-year encodings are stacked into a multi-channel grid. The grid is partitioned into fixed-size patches and linearly projected into patch embeddings, which are combined with spatial positional encodings. Together with temporal query tokens representing the forecast horizon ($t+1$), these embeddings are processed by a Transformer encoder with multi-head self-attention. The output query tokens are mapped back to patch-level residuals, assembled into a grid-based displacement map, and added to the last observed displacement. After de-normalisation, this yields the final single-step forecast in millimetres.

All networks are trained with the AdamW optimiser, using a linearly increasing learning-rate warm-up followed by cosine decay, gradient clipping, and automatic mixed precision. We also maintain an exponential moving average (EMA) of the model weights and use the EMA parameters for validation and testing, which reduces the variance of the estimates and leads to more stable convergence in practice. Early stopping based on validation loss is employed to prevent overfitting, and model selection for all architectures is carried out under the unified evaluation protocol described in Section 4.

3.5. Training regimes and cross-site setup

The proposed preprocessing pipeline and multimodal representation (Sections 2–3) are applied consistently to all EGMS tiles considered in this study. We distinguish three training regimes, which correspond to the main groups of experiments reported in Section 4.

In-tile training on eastern Ireland. For the core model comparison and ablation studies we train all architectures (CNN–LSTM, CNN–LSTM+Attn, MM–STGCN and the proposed multimodal transformer) on tile E32N34 covering eastern Ireland. The data cube is split chronologically into 80% training and 20% validation/test samples as described in Sections 2 and 3. All models are trained from scratch on this tile only, and hyperparameters are selected on its validation set under the unified optimisation strategy of Section 3.4.

We further perform an ablation in which all multimodal models are trained under a simple SmoothL1 objective; see Section 5.3.1.

Cross-site generalisation across Europe. To assess whether the learned multimodal representation and transformer architecture transfer across distinct deformation regimes, we perform cross-site generalisation experiments. A single multimodal transformer is trained on tile E32N34 (source tile) only, with early stopping based on its validation loss. The resulting model is then applied without any fine-tuning to a set of target tiles (E39N30, E44N23, E32N35, E48N24, E58N17), which cover continuous subsidence, periodic deformation and abrupt

co-seismic displacement. For these experiments the normalisation parameters for both displacement and static indicators are estimated on the source tile and reused unchanged for all target tiles (Section 3.2), so that the network sees input statistics that are consistent with those encountered during training.

Site-specific training on representative deformation regimes.. In addition to zero-shot cross-site transfer, we also investigate how well the proposed transformer can be specialised to individual regions when local training data are available. For each of the above tiles we construct a local dataset using the same preprocessing, multimodal feature construction and 80/20 temporal split as for E32N34. A separate transformer is then trained from scratch on each tile and evaluated on its held-out test portion. Comparing these site-specific models with the cross-site generalisation results provides insight into (i) how much performance is gained by local retraining, and (ii) which deformation regimes are intrinsically more challenging to predict given the EGMS time series.

4. Experiments

4.1. Experimental setup

4.1.1. Prediction task and data split

All experiments address single-step prediction of ground deformation using the EGMS Level 3 Upward component (Section 2). Given a sequence of T_{in} past observations and auxiliary variables, the models are trained to predict the displacement map at the next epoch,

$$\hat{d}_{t+1} = f_{\theta}(\mathbf{X}_{t-T_{in}+1:t}), \quad (20)$$

where $\mathbf{X}_{t-T_{in}+1:t}$ denotes either the displacement-only or the multimodal input described in Section 3, and θ are learnable parameters.

Training samples are constructed by sliding a fixed-length window along each EGMS time series and discarding incomplete windows at the beginning and end of the acquisition period. For every tile, the time series are split chronologically: the first 80 % of epochs are used for training and the remaining

20 % for validation and testing. All reported numbers are computed on this held-out temporal segment, so that models are always evaluated on future epochs that were never seen during training.

For the core model comparison we consider tile E32N34 (eastern Ireland). Cross-site experiments follow the regimes defined in Section 3.5, covering additional EGMS tiles across Europe that represent distinct deformation types (continuous subsidence, seasonal motion and abrupt co-seismic offsets).

4.1.2. Input configurations

We evaluate two input configurations:

1. **Displacement-only (unimodal).** The input at each time step consists solely of the EGMS displacement map, normalised per-pixel as described in Section 3.2. This setting mirrors the configuration investigated in our previous work [15] and serves as a reference for pure time-series deformation forecasting.
2. **Multimodal (proposed).** In addition to the displacement map, the input stack contains three static fields (mean velocity, linear acceleration and seasonal amplitude) and a two-dimensional temporal encoding $(\sin \phi_t, \cos \phi_t)$ of the day-of-year. All channels are jointly interpolated to a common 64×64 grid and normalised. The resulting six-channel tensor allows the models to exploit long-term kinematics and seasonal cycles even though the prediction horizon is one step.

Unless otherwise stated, all architectures use the same pre-processing pipeline and the same temporal train/validation split in both configurations. The only difference between the two settings is the number of channels provided to the networks.

4.1.3. Training and evaluation protocol

All models are implemented in PyTorch. For the CNN-LSTM and CNN-LSTM+Attention baselines we follow common settings for spatio-temporal sequence modelling [17]. The MM-STGCN uses two spatio-temporal blocks with an 8-neighbour regular grid graph over the 64×64 pixels, as detailed in Section 3. The proposed multimodal transformer is trained with the composite loss of Section 3.4, combining per-pixel ℓ_1 loss, relative error in millimetres, correlation and gradient regularisation in a residual-prediction setting.

All networks are optimised with Adam or AdamW, using learning-rate warm-up followed by cosine decay, gradient clipping and automatic mixed precision. We maintain an exponential moving average (EMA) of the model parameters and use the EMA weights for validation and testing. Early stopping on the validation loss is employed in all cases.

We report root-mean-square error (RMSE), mean absolute error (MAE) and coefficient of determination (R^2) computed over all pixels and time steps in the test set. In addition, we use threshold-based accuracies:

- relative thresholds $\text{Acc}@10\%, 20\%, 50\%$, defined as the fraction of pixels whose absolute error is below 10 %, 20 %, 50 % of the true displacement magnitude;

Table 2: Single-step prediction performance on tile E32N34 with displacement-only inputs. Best values are highlighted in bold.

Model	RMSE [mm]	MAE [mm]	R^2
Linear trend	2.1041	1.1933	0.8428
Linear + seasonal harmonic	2.0168	1.1451	0.8555
CNN-LSTM	2.0239	1.3442	0.8621
CNN-LSTM+Attn	1.8230	1.1268	0.8881
STGCN	1.0410	0.6957	0.9635
Transformer (ours)	1.5873	0.9389	0.9152

- absolute thresholds in millimetres, $\text{Acc}@1\text{mm}, 0.5\text{mm}, 0.2\text{mm}, 0.1\text{mm}$, defined as the fraction of pixels whose absolute error is below the corresponding level.

For qualitative assessment we also compute the structural similarity index (SSIM) and Pearson correlation between predicted and reference maps, and visualise scatter plots and residual diagnostics.

4.2. Model comparison on eastern Ireland (E32N34)

4.2.1. Displacement-only baseline

We first compare two simple geodetic baselines with the four deep architectures when only displacement maps are used as input. The classical baselines operate independently on each pixel time series: (i) a linear trend model fitted over the training period and extrapolated one step ahead, and (ii) a linear trend plus seasonal harmonic model using a single annual sinusoid. Table 2 summarises the single-step prediction performance on tile E32N34 in this unimodal setting.

The two classical baselines provide a useful lower bound on performance: the linear trend and linear-plus-seasonal models reach $\text{RMSE} \approx 2.1$ mm and $\text{RMSE} \approx 2.0$ mm, respectively, with R^2 between 0.84 and 0.86. All deep models improve upon these geodetic baselines in terms of global error and explained variance. Among the neural architectures, STGCN clearly provides the strongest performance when only displacement history is available, achieving an RMSE of 1.04 mm and an R^2 of 0.96. The proposed transformer attains an RMSE of 1.59 mm and $R^2 = 0.92$, outperforming both CNN-LSTM variants but remaining behind STGCN in this configuration.

Threshold accuracies in Table 3 provide additional insight. The classical baselines already achieve reasonable fractions of pixels within 1 mm absolute error (around 60–61%), but still lag behind STGCN and the transformer at the strictest thresholds. STGCN attains the highest fraction of pixels within 1 mm and 0.5 mm, while the transformer yields the best performance in the most demanding $\text{Acc}@0.1\text{mm}$ bin.

Figure 3 shows a representative example of predicted displacement maps for all models. All architectures reproduce the broad coastal subsidence bowl, but STGCN and the transformer exhibit higher structural fidelity than the CNN-LSTM baselines, with SSIM and map-wise correlation close to 0.98 on this epoch and clearly sharper structures than those implied by the pixel-wise classical regressions.

Table 3: Threshold accuracies on tile E32N34 for displacement-only inputs. Values are given in percent.

Model	Acc@10%	Acc@20%	Acc@50%	Acc@1mm	Acc@0.5mm	Acc@0.2mm	Acc@0.1mm
Linear trend	33.77	46.29	69.38	59.99	41.65	28.43	23.75
Linear + seasonal harmonic	34.72	47.65	70.26	61.48	42.81	28.89	24.01
CNN-LSTM	11.94	23.37	48.74	54.37	32.24	13.76	6.90
CNN-LSTM+Attn	14.19	27.50	53.57	61.26	42.70	26.45	15.69
STGCN	24.66	40.83	61.52	76.15	54.51	34.32	10.78
Transformer (ours)	16.16	31.92	59.24	67.58	46.76	27.97	16.87

Table 4: Single-step prediction performance on tile E32N34 with multimodal inputs (displacement + static kinematics + temporal encoding).

Model	RMSE [mm]	MAE [mm]	R^2
CNN-LSTM (Multi)	1.9704	1.1721	0.8693
CNN-LSTM+Attn (Multi)	1.9112	1.1579	0.8770
MM-STGCN	1.4465	0.7299	0.9295
Transformer (ours, Multi)	0.9007	0.5738	0.9727

4.2.2. Multimodal conditioning on static and temporal covariates

We next enable the full multimodal input (displacement + static kinematics + temporal encoding) for all models. The corresponding quantitative results on E32N34 are reported in Table 4.

Augmenting the input with static and temporal covariates substantially changes the relative ranking. The multimodal transformer now achieves the best performance, with an RMSE of 0.90 mm and $R^2 = 0.97$, outperforming the multimodal STGCN (RMSE 1.45 mm, $R^2 = 0.93$) and both CNN-LSTM variants. Compared with its displacement-only counterpart, the transformer’s RMSE decreases by roughly 40 % and the explained variance increases from 0.92 to 0.97.

Table 5 reports the threshold accuracies for the multimodal setting. All architectures benefit from the enriched inputs, but the gains are most pronounced for the transformer: Acc@10 % almost triples (from 16.2 % to 47.2 %), and the proportion of predictions within 1 mm increases from 67.6 % to 81.0 %.

Qualitative maps in Figure 4 illustrate the impact of multimodal conditioning. The transformer predictions are visually almost indistinguishable from the EGMS reference, with SSIM and map-wise correlation close to 0.99 and the smallest residuals in both the coastal subsidence bowl and the more stable inland areas. The multimodal STGCN also yields sharper structures than its unimodal version, but exhibits a slight amplitude bias in the highest-subsidence zones. Residual diagnostics and binned error statistics (see Figure 5(b)) show that the multimodal transformer maintains stable accuracy across the full deformation range, with narrow residual distributions even in the largest-magnitude bins.

4.3. Cross-site experiments across Europe

We now turn to the six EGMS tiles introduced in Section 2, which were selected to span three deformation regimes: continuous subsidence (E39N30, E44N23), seasonal deformation

(E32N34, E32N35) and abrupt co-seismic offsets (E48N24, E58N17). All experiments in this subsection use the multimodal input configuration and the transformer architecture.

4.3.1. Site-specific multimodal training

In the first set of experiments, we train a separate multimodal transformer from scratch on each tile, following the site-specific regime in Section 3.5. Table 6 summarises the single-step performance on the held-out test portion of each time series.

Across all tiles and deformation regimes, the site-specific multimodal transformer attains high coefficients of determination ($R^2 \geq 0.93$ for all seasonal and continuous-subsidence sites, $R^2 \approx 0.99$ for the co-seismic case E58N17), with between 70 % and 80 % of pixels within 1 mm error for the seasonal and continuous sites. In co-seismic areas, absolute errors in millimetres are higher due to the larger signal amplitudes, but the relative errors remain small and R^2 values very close to 1, indicating that the transformer can reproduce both the location and the shape of abrupt displacement fields.

4.3.2. Cross-site generalisation from eastern Ireland

To quantify cross-site generalisation, we next train a single multimodal transformer only on tile E32N34 (eastern Ireland) and evaluate it without any fine-tuning on the remaining five tiles, as described in Section 3.5. For these experiments, the normalisation parameters (per-pixel displacement statistics and per-channel static descriptors) are estimated on E32N34 and reused for all other tiles, so that the model sees input statistics consistent with its training environment.

Table 7 reports the zero-shot performance of this E32N34-trained transformer across all six tiles.

Several observations emerge. First, the cross-site transformer achieves $R^2 \geq 0.93$ on all target tiles, despite never seeing their data during training and using normalisation statistics from a different region. For the seasonal and continuous-subsidence sites, RMSE values remain close to or below 1 mm and Acc@1mm ranges between 74 % and 81 %, only moderately lower than the site-specific models in Table 6. Second, the transformer also attains high overall R^2 and competitive threshold accuracies on the two co-seismic tiles (E48N24 and E58N17). However, these aggregate scores must be interpreted with care. Our task is one-step-ahead nowcasting: for each prediction $\hat{d}_{t+1|1:t}$ the input history window contains observations only up to epoch t . Therefore, the abrupt co-seismic

Table 5: Threshold accuracies on tile E32N34 for multimodal inputs. Values are given in percent.

Model	Acc@10%	Acc@20%	Acc@50%	Acc@1mm	Acc@0.5mm	Acc@0.2mm	Acc@0.1mm
CNN-LSTM (Multi)	25.74	43.51	71.44	59.98	41.83	28.50	23.84
CNN-LSTM+Attn (Multi)	29.96	44.43	72.03	59.84	41.59	28.35	23.67
MM-STGCN	28.89	58.21	80.70	75.05	53.29	33.78	26.46
Transformer (ours, Multi)	47.22	63.69	82.37	81.01	59.31	37.19	28.39

Table 6: Site-specific multimodal transformer performance for representative EGMS tiles. Each model is trained and evaluated on a single tile using the 80/20 temporal split.

Tile ID	Deformation type	RMSE [mm]	MAE [mm]	R^2	Acc@1mm [%]
E32N34	Seasonal / mixed	0.9007	0.5738	0.9727	81.01
E32N35	Seasonal	1.0352	0.6290	0.9251	79.22
E39N30	Continuous subsidence	1.1199	0.7580	0.9516	75.56
E44N23	Continuous subsidence	1.4100	0.9089	0.9508	69.78
E58N17	Co-seismic (Croatia)	4.0497	2.5462	0.9882	48.92

offset at the event epoch cannot be anticipated unless it has already been observed in the input sequence. In practice, the event enters the input window only *after* the first post-event acquisition, and the model performance over the long post-seismic period largely reflects its ability to remain numerically stable and to update its forecasts once the discontinuity has occurred.

To make this explicit, Figure 7 reports representative pixel-wise time series for both co-seismic tiles, together with their one-step predictions and the event-centred error curves. The plots show an unavoidable error peak around the estimated event epoch, followed by stable behaviour afterwards once the post-seismic level becomes part of the conditioning history. Hence, the transfer results on co-seismic tiles should be understood as *robustness to strong discontinuities and rapid post-event updating*, rather than the prediction of earthquake occurrence.

Figure 6 illustrates qualitative examples of *zero-shot cross-tile transfer* for single-step ($t+1$) forecasting. A multimodal Transformer trained only on tile E32N34 is applied to the other tiles *without any fine-tuning or retraining*, so the figure visualises transferability rather than site-specific accuracy.

To verify that the strong cross-site performance is not a generic property of the data or of any reasonably regularised model, we also evaluate a multimodal STGCN trained only on tile E32N34 and applied zero-shot to the same set of target tiles (Table 7). In this setting the STGCN exhibits noticeably weaker generalisation: for the continuous-subsidence tiles E39N30 and E44N23, RMSE increases to 1.8 to 2.2 mm and Acc@1mm drops to 41–49%, while for the co-seismic tiles the errors become substantially larger (RMSE > 6 mm on E48N24 and > 8 mm on E58N17) and fewer than one third of pixels fall within 1 mm of the reference displacement.

Compared to the transformer in Table 7, which maintains RMSE close to or below 1 mm and Acc@1mm between 71% and 81% on most tiles, these results indicate that cross-site generalisation is not trivial and strongly depends on the model

architecture. The multimodal transformer retains much of its site-specific skill when transferred to unseen regions, whereas the STGCN, despite being competitive in the single-site experiments, degrades more severely when exposed to distribution shifts in deformation regime and noise characteristics.

4.4. Summary of experimental findings

Overall, the experiments can be summarised as follows:

- On a single tile (E32N34), STGCN is the strongest architecture when only displacement maps are available, while the proposed multimodal transformer becomes the top performer once static and temporal covariates are included, reducing RMSE by about 40% relative to its unimodal counterpart and surpassing STGCN in both global metrics and threshold accuracies.
- Across six EGMS tiles spanning continuous, seasonal and co-seismic deformation, site-specific multimodal transformers systematically achieve high R^2 and robust Acc@1mm, confirming that the architecture can adapt to very different deformation regimes.
- A single multimodal transformer trained on eastern Ireland generalises surprisingly well to all other tiles without fine-tuning, maintaining $R^2 \geq 0.93$ and Acc@1mm in the 70–80% range. Performance for co-seismic tiles is particularly strong in relative terms.

These empirical results form the basis for the broader interpretation and implications discussed in Section 5.

5. Discussion

5.1. Impact of multimodal conditioning on single-tile forecasting

The experiments on the eastern Ireland tile (E32N34) demonstrate that augmenting EGMS displacement time series with

Table 7: Cross-site generalisation of a multimodal Transformer and a multimodal STGCN trained only on tile E32N34 and evaluated without fine-tuning on the other five tiles. All inputs are normalised using statistics from E32N34.

Tile ID	Deformation type	Model	RMSE [mm]	MAE [mm]	R^2	Acc@1mm [%]
E32N34 (source)	Seasonal / mixed	Transformer (ours)	0.7353	0.4092	0.9811	87.37
		MM-STGCN	1.0178	0.6684	0.9651	76.77
E32N35	Seasonal	Transformer (ours)	0.9996	0.5743	0.9301	80.40
		MM-STGCN	1.5341	1.0772	0.8404	58.82
E39N30	Continuous subsidence	Transformer (ours)	0.9699	0.5799	0.9637	81.20
		MM-STGCN	1.8133	1.3437	0.8778	48.54
E44N23	Continuous subsidence	Transformer (ours)	1.2670	0.7826	0.9603	74.93
		MM-STGCN	2.1748	1.6278	0.8872	40.73
E48N24	Co-seismic (Samos)	Transformer (ours)	3.1777	1.0219	0.9729	73.19
		MM-STGCN	6.6834	2.9453	0.8807	32.23
E58N17	Co-seismic (Croatia)	Transformer (ours)	1.5520	0.8047	0.9983	71.40
		MM-STGCN	8.3652	6.3216	0.9513	15.08

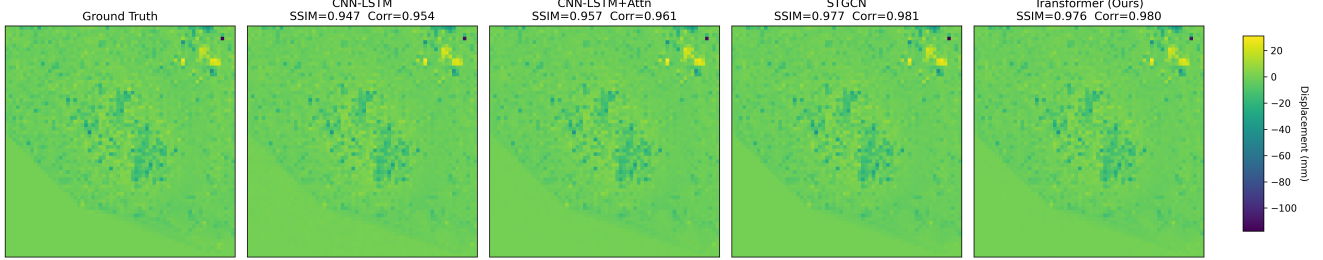


Figure 3: Single-step predicted displacement map comparison for the displacement-only setting on tile E32N34.

static kinematic descriptors and harmonic time encodings substantially improves the accuracy and robustness of single-step ground-motion forecasting. When only displacement maps are used as input (Section 4), the STGCN baseline achieves the best performance among the four architectures with an $RMSE = 1.04$ mm and $R^2 = 0.96$, while the proposed Transformer obtains $RMSE = 1.59$ mm and $R^2 = 0.92$. In other words, with purely kinematic information the graph-based model benefits more from its strong spatial inductive bias than the more flexible but less constrained attention architecture.

Once mean velocity, acceleration, seasonal amplitude and harmonic day-of-year encodings are included (Section 4), the ranking is reversed. The multimodal Transformer reaches $RMSE = 0.90$ mm, $MAE = 0.57$ mm and $R^2 = 0.97$, clearly outperforming the multimodal STGCN ($RMSE = 1.45$ mm, $R^2 = 0.93$) and both CNN-LSTM variants. The recurrent baselines also benefit from the additional channels, but the absolute gains are modest and do not fundamentally change their relative position. This shift highlights that self-attention particularly benefits from rich feature spaces: with displacement-only input, the Transformer must infer long-term trends, seasonal cycles and short-term anomalies purely from local temporal context, whereas with multimodal conditioning these factors are at least partially disentangled and presented explicitly as separate channels.

5.2. Threshold accuracies and practical relevance

Threshold accuracies provide a more operational view of the forecasting skill, especially for applications that rely on displacement exceedance criteria. In the displacement-only configuration, the STGCN achieves the highest $Acc@1mm$ (about 76%), whereas the Transformer reaches roughly 68%, with both models outperforming the CNN-based baselines across most thresholds. After multimodal conditioning, the Transformer exhibits the largest relative improvement: $Acc@1mm$ increases to 81%, and the proportion of pixels within 10% relative error nearly triples compared with the unimodal case (Section 4). The multimodal STGCN also improves, but remains behind the Transformer at the tightest thresholds (0.5 mm and below).

These gains are particularly relevant for asset-management and near-real-time monitoring scenarios, where the key question is not only how small the global $RMSE$ is, but how reliably a model remains within narrow bands around physically meaningful limits from one acquisition to the next. In this sense, the proposed single-step predictor is best viewed as providing short-range updates between consecutive EGMS epochs, which can complement dedicated early-warning systems that operate on different time scales and with additional information (e.g. hydrological or engineering data).

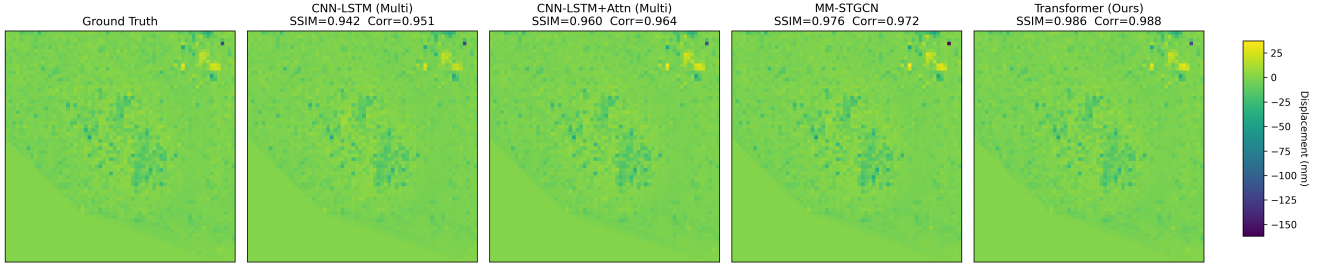
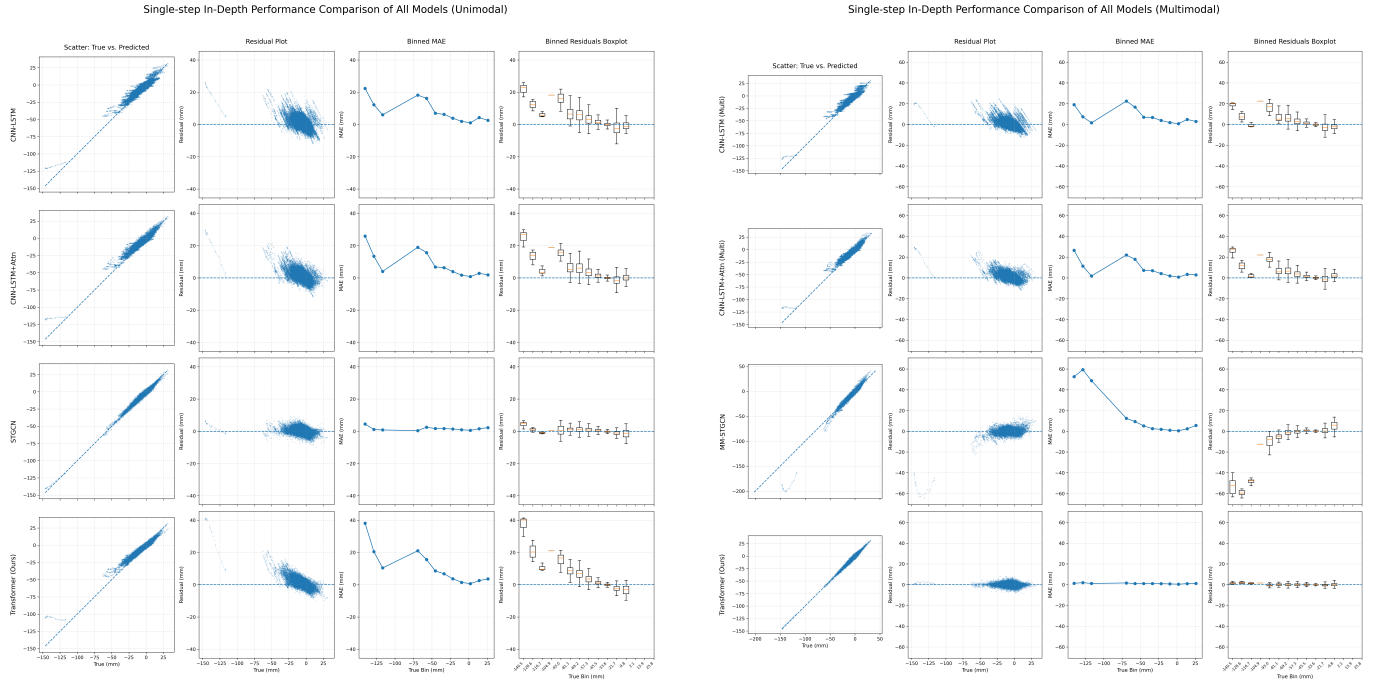


Figure 4: Single-step predicted displacement map comparison for the multimodal setting on tile E32N34.



(a) In-depth performance analysis for all models in the displacement-only setting.

(b) In-depth performance analysis for all models in the multimodal setting.

Figure 5: Comparison between unimodal and multimodal performance analyses on tile E32N34.

5.3. Error structure and deformation regimes

The map-based comparisons in Figures 3 and 4 show that all four architectures reproduce the broad deformation pattern over eastern Ireland, but differ in structural detail. In the displacement-only case, STGCN and the Transformer achieve the highest SSIM and pixel-wise correlation with the reference EGMS map, indicating that both capture the morphology of subsidence bowls and stable areas reasonably well. However, the deep-analysis panel for the unimodal setting (Figure 5(a)) reveals clear magnitude-dependent biases: CNN-based models tend to under-estimate large subsidence, while the Transformer exhibits more dispersed residuals at intermediate magnitudes.

In the multimodal configuration, the Transformer delivers the most faithful reconstruction of fine-scale deformation structures. Its predicted maps are visually closest to the ground truth, and the associated SSIM and correlation scores are highest across the four architectures. The residual analysis in Fig-

ure 5(b) shows that Transformer errors are tightly concentrated around zero with a nearly flat binned-MAE curve, suggesting stable accuracy across the full displacement range. The multimodal STGCN remains competitive, particularly in smoothly varying regions, but exhibits slightly broader residual distributions and more skewness in the largest-subsidence bins. These patterns support the hypothesis that global self-attention is especially effective at reconciling signals from static and dynamic modalities and at propagating information across the entire spatial domain.

5.3.1. Ablation on loss functions

A potential concern is that the proposed Transformer is trained with a richer composite loss (Section 3.4) than the baselines, which might favour it on structural metrics and threshold-based accuracies. To assess whether our conclusions depend on this choice, we conduct an ablation in which both the multi-

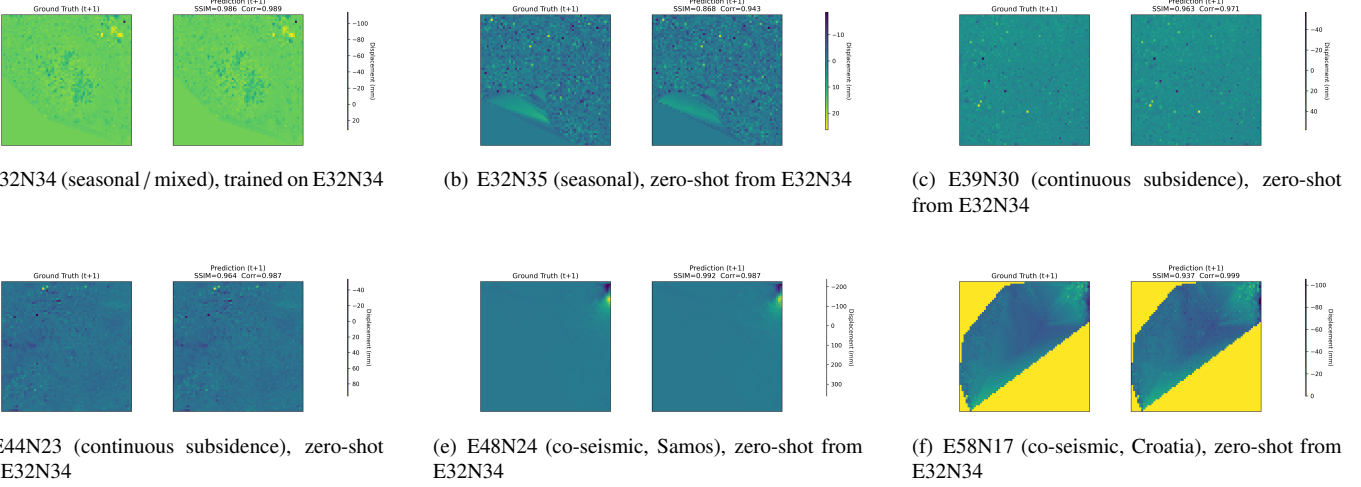


Figure 6: Qualitative examples of *zero-shot* cross-tile single-step ($t+1$) forecasts. The multimodal Transformer is trained only on tile E32N34 (eastern Ireland) and applied to the other tiles *without fine-tuning*. Each panel shows the ground truth at $t+1$ (left) and the prediction (right), covering seasonal deformation (E32N35), continuous subsidence (E39N30, E44N23) and co-seismic offsets (E48N24, E58N17).

Table 8: Ablation on loss functions for multimodal single-step forecasting on tile E32N34. All models use identical inputs, training splits and optimisation settings; only the loss definition differs.

Model & loss	RMSE [mm]	MAE [mm]	R^2	Acc@1mm [%]
MM-STGCN (SmoothL1 only)	1.0178	0.6684	0.9651	76.77
Transformer (SmoothL1 only)	0.8701	0.5514	0.9737	82.12
Transformer (composite loss)	0.7353	0.4092	0.9811	87.37

modal Transformer and the multimodal STGCN are retrained on tile E32N34 using a simple SmoothL1 loss only, i.e. without the relative-error, correlation or gradient terms.

Table 8 summarises the single-step performance under this setting. Even when trained solely with SmoothL1 loss, the Transformer clearly outperforms MM-STGCN: RMSE is reduced from 1.02 mm to 0.87 mm, MAE from 0.67 mm to 0.55 mm, and R^2 improves from 0.97 to 0.97 (from 0.965 to 0.974 in absolute terms). The proportion of predictions within 1 mm also increases from 76.8% to 82.1%.

For reference, we also include the Transformer trained with the full composite loss. As expected, the additional terms further decrease the error (RMSE 0.74 mm, MAE 0.41 mm, $R^2 = 0.98$) and increase Acc@1mm to 87.4%, but they are not required for the Transformer to surpass MM-STGCN. This ablation confirms that the superior multimodal performance of the proposed architecture is not an artefact of using a more complex loss function.

5.4. Cross-site behaviour and generalisation across Europe

The additional experiments on six EGMS tiles representing contrasting deformation regimes (continuous subsidence, seasonal motion and co-seismic offsets; Section 4.3 and Figure 6) provide a first assessment of how the multimodal Transformer behaves beyond the original training tile.

We note that the set of representative EGMS tiles overlaps with our related study [16], but the experimental regime differs

fundamentally: there models are trained in a site-specific manner, whereas here we evaluate *zero-shot* transfer from a single source tile (E32N34) without retraining.

When the model is re-trained separately on each tile using the same architecture and preprocessing, it achieves consistently high single-step skill across all sites, with R^2 values typically between 0.93 and 0.99 and Acc@1mm commonly exceeding 70% in both continuous and seasonal settings. Even in the challenging co-seismic tiles affected by the Samos and Croatia earthquakes, the Transformer maintains high R^2 and very high Acc@50%, indicating that it can capture both the amplitude and spatial footprint of abrupt offsets once site-specific statistics are provided.

More importantly for the broader theme of this work, the zero-shot experiments—where a single multimodal Transformer trained only on E32N34 is applied without fine-tuning to the other five tiles—show that much of this skill carries over across Europe. Across all six sites (including E32N34 itself), the zero-shot model attains $R^2 \geq 0.93$, with Acc@1mm typically in the range of 70–80% for continuous and seasonal regimes and slightly lower but still competitive values for the co-seismic cases. Tiles dominated by seasonal or trend-like behaviour (e.g. E32N35, E39N30, E44N23) show particularly strong transfer, whereas large, step-like co-seismic offsets expose the natural limitations of training on a single, comparatively smooth reference tile. For the co-seismic tiles, it is important to distinguish between forecasting an event and being robust to its consequences. Because our model performs one-step-ahead nowcasting, it does not have access to physical precursors of an earthquake and cannot predict the co-seismic jump *before* it occurs. Instead, its apparent strong performance over co-seismic records is mainly driven by the post-event period, during which the input window already includes the new displacement level. Figure 7 visualises this behaviour: errors peak at the event epoch and then remain bounded afterwards, illustrating robustness to sharp discontinuities rather than earth-

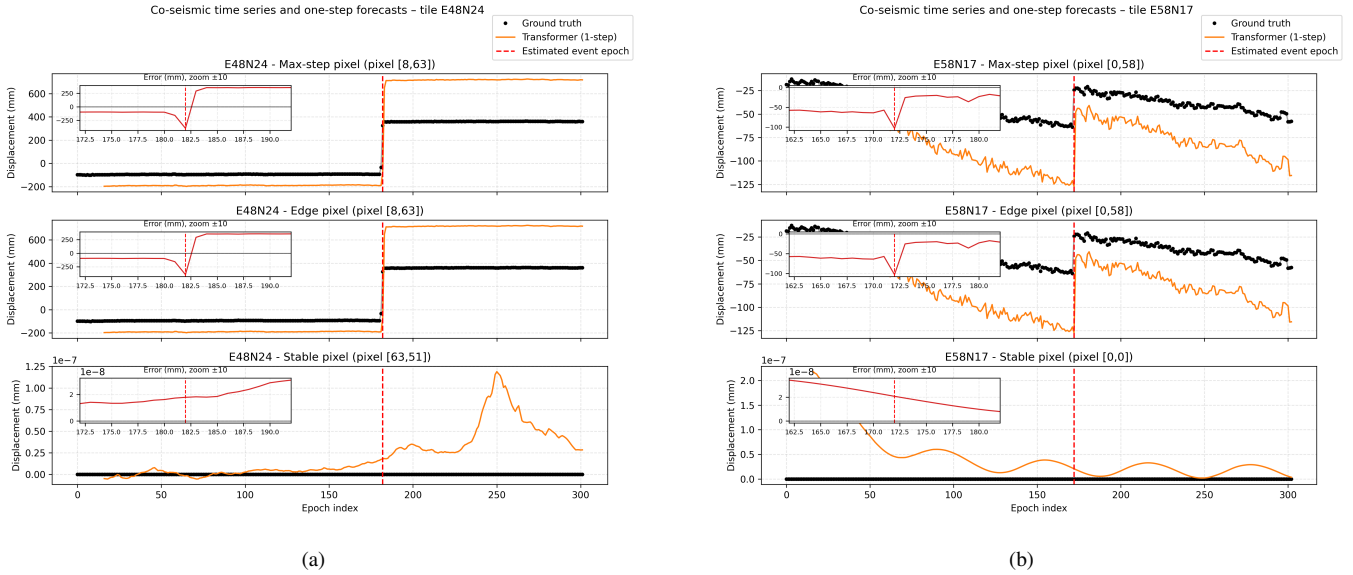


Figure 7: Event-centred interpretation of co-seismic ‘forecasting’ in the zero-shot setting. For each co-seismic tile (E48N24: Samos; E58N17: Croatia), we show three representative pixels (largest step, step-edge, and a stable/background pixel). Black markers denote EGMS displacement time series, and the orange curve is the multimodal Transformer one-step-ahead nowcast $\hat{d}_{t+1|1:t}$ produced by sliding the input history window through time. The red dashed line indicates the estimated co-seismic epoch (largest absolute one-step change), and the inset in each panel plots the prediction error (prediction minus truth) in a ± 10 epoch window around the event. As expected for a single-step forecaster trained on smooth deformation histories, the model does not anticipate the abrupt jump and exhibits a sharp error peak at the co-seismic epoch; after the discontinuity is observed and enters the conditioning history, the predictions remain stable and track the post-event state.

quake prediction.

The additional cross-site experiments with a multimodal STGCN trained on E32N34 further support this interpretation: although STGCN performs very well in the site-specific setting, its zero-shot transfer to other tiles leads to markedly larger errors and much lower threshold accuracies than those of the transformer. This suggests that the global self-attention and query-token design of the multimodal transformer provides a more robust inductive bias for handling regional shifts in deformation regime and noise characteristics than purely local spatio-temporal graph convolutions.

Taken together, these results suggest that the proposed multimodal design does not merely overfit to one specific region, but learns deformation patterns and modality interactions that are reusable across sites with different kinematic regimes. At the same time, the gap between per-tile and zero-shot performance, especially in co-seismic settings, highlights the value of lightweight fine-tuning or domain-adaptation strategies when moving to strongly out-of-distribution areas.

5.5. Role of architectural choices

The comparison between CNN-LSTM, CNN-LSTM+Attn, STGCN and the Transformer clarifies the respective strengths of recurrent, graph and attention-based designs for InSAR-driven deformation forecasting. The consistent but moderate improvement of CNN-LSTM+Attn over the plain CNN-LSTM in all configurations indicates that simple additive temporal attention helps recurrent networks to focus on informative historical states, but does not fundamentally change their capacity to model complex spatio-temporal dependencies.

STGCN excels in the displacement-only setting because it hard-codes the regular grid topology and performs local message passing over neighbouring pixels. This inductive bias aligns well with the spatial continuity of displacement fields and acts as an effective regulariser when auxiliary inputs are absent. The Transformer, in contrast, treats each patch as a token and relies on learned positional encodings; its flexibility is most advantageous when multiple modalities and longer temporal contexts must be integrated, but can be less data-efficient in the purely unimodal regime.

The multimodal Transformer configuration adopted here—patch-wise encoding, temporal query tokens, residual prediction in normalised space, and a composite loss balancing absolute, relative, structural and incremental errors—appears to strike a favourable balance between expressivity and stability. Query tokens decouple the representation of future states from the input sequence, residual learning focuses the network on short-term increments rather than absolute levels, and pixel-wise normalisation ensures that subsidence bowls, seasonal cycles and co-seismic steps are treated on comparable scales. The strong multimodal and cross-site performance suggests that these architectural choices are well suited to dense EGMS-like data.

5.6. Implications for operational ground-motion monitoring

From an application perspective, the results indicate that multimodal learning has practical value for operational deformation monitoring workflows based on EGMS or similar InSAR products. Within the constraints of single-step prediction at the Sentinel-1 repeat interval, the multimodal Transformer can provide map-wide forecasts of likely displacement at the

next acquisition, which is useful for tracking whether ongoing trends are accelerating, stabilising or remaining within expected bounds. Static descriptors of historical displacement (mean velocity, acceleration, seasonal amplitude) can be computed once from archived time series and re-used as low-cost covariates, while harmonic time encodings inject seasonal phase information without requiring external forcing data.

The fact that a single multimodal Transformer trained on one tile generalises reasonably well across other European sites suggests that a continental-scale forecasting system could be built around a small number of pre-trained models, optionally fine-tuned on regions of special interest. High accuracies at tight thresholds further indicate that such models could support prioritisation of areas for more frequent acquisitions, detailed geotechnical inspection or targeted modelling, particularly where small deviations from background subsidence trends are operationally significant.

5.7. Limitations and future work

Despite these promising results, several limitations remain. First, the training and primary comparison are still centred on a single EGMS tile in eastern Ireland, and the cross-site experiments, although covering different deformation regimes, are restricted to a small set of European examples. A broader evaluation over a more diverse collection of tiles, including rapidly subsiding megacities, volcanic regions and landslide-prone slopes, would provide a more comprehensive picture of the model’s strengths and failure modes. In this context, systematic studies of zero-shot transfer, fine-tuning and domain adaptation will be an important next step.

Second, the present framework focuses on single-step forecasting at a fixed temporal resolution. Extending the approach to multi-step horizons and irregular sampling, and integrating it into real-time updating pipelines, would increase its utility for early-warning and decision-support systems. A more explicit treatment of predictive uncertainty—for example via quantile regression, ensembles or Bayesian variants of the Transformer—would further enhance its suitability for risk-informed applications.

Finally, the multimodal inputs considered here represent only a subset of potentially informative covariates. Incorporating additional data layers such as digital elevation models, land cover, groundwater levels or anthropogenic loading indicators could both improve forecast skill and help disentangle different physical drivers of deformation. Combining the proposed Transformer with interpretability tools (e.g. SHAP values, attention visualisation or gradient-based saliency) will be essential to understand which modalities, spatial regions and time periods dominate its predictions, and to bridge the gap between purely data-driven learning and process-based geophysical understanding.

Overall, the discussion above highlights that multimodal attention-based models offer a promising and flexible framework for high-precision land-deformation forecasting from satellite-derived ground-motion products, while also pointing to clear avenues for further validation and methodological refinement.

6. Conclusions and outlook

This study presented a multimodal deep learning framework for single-step ground-deformation forecasting from European Ground Motion Service (EGMS) Level 3 products. Building on a displacement-only benchmark developed in our previous work, we constructed a unified six-channel input representation that combines dynamic displacement history, static descriptors of long-term kinematics and harmonic time-of-year encodings, and evaluated four representative spatio-temporal architectures—CNN-LSTM, CNN-LSTM with temporal attention, a spatio-temporal graph convolutional network (STGCN), and a patch-based multimodal Transformer—on an EGMS tile covering eastern Ireland. We then extended the analysis to a set of additional tiles across Europe representing continuous subsidence, seasonal motion and co-seismic displacement.

Our main findings can be summarised as follows:

1. **Multimodal conditioning substantially improves predictive skill.** Across all architectures, enriching the displacement time series with static deformation statistics and harmonic day-of-year information yields more accurate and more reliable forecasts than using displacement maps alone. The effect is particularly pronounced for the Transformer: when moving from the displacement-only to the multimodal setting on the eastern Ireland tile, its RMSE decreases from about 1.6 mm to 0.9 mm and R^2 increases from roughly 0.92 to 0.97, with threshold accuracies improving systematically from Acc@10% down to Acc@0.1mm.
2. **A tailored multimodal Transformer outperforms specialised spatio-temporal baselines.** In the displacement-only experiments, the STGCN baseline achieves the best overall accuracy, reflecting the advantage of exploiting explicit grid topology and local message passing when only kinematic information is available. In the multimodal configuration, however, the proposed Transformer—combining patch-wise embeddings, temporal query tokens and residual prediction in normalised space—consistently outperforms the multimodal STGCN and both CNN-LSTM variants in terms of RMSE, R^2 and threshold-based accuracy. Qualitative comparisons and structural similarity metrics confirm that the multimodal Transformer provides the most faithful reconstructions of fine-scale deformation patterns.
3. **Attention mechanisms are particularly effective in rich feature spaces.** The moderate but consistent gain of CNN-LSTM+Attn over the plain CNN-LSTM indicates that even simple temporal attention helps recurrent models focus on informative historical states. The much larger gains achieved by the multimodal Transformer suggest that global self-attention is especially powerful when the model must fuse heterogeneous spatially distributed inputs (dynamic displacement, static summary statistics and temporal encodings) and propagate information across the

full spatial domain. In this regime, attention-based architectures are not only competitive with, but can surpass, state-of-the-art spatio-temporal graph models.

4. **The multimodal Transformer generalises across European deformation regimes.** Additional experiments on six EGMS tiles representing continuous subsidence, seasonal ground motion and co-seismic offsets show that the proposed architecture maintains high single-step skill well beyond the original training tile. When re-trained per site, the multimodal Transformer attains R^2 values typically between 0.93 and 0.99 with Acc@1mm often above 70% across all regimes. In a stricter zero-shot setting, a single model trained only on the eastern Ireland tile still achieves $R^2 \geq 0.93$ and competitive threshold accuracies on the remaining tiles, indicating that it learns deformation patterns and modality interactions that transfer across diverse European settings.

From an operational perspective, these results indicate that multimodal attention-based models constitute a promising tool for EGMS-based deformation monitoring. The additional inputs required in this work (long-term velocity, acceleration, seasonal amplitude and sinusoidal time features) can be derived directly from existing InSAR stacks without external data, making the proposed approach straightforward to integrate into current processing pipelines. The high accuracies achieved at strict absolute and relative error thresholds, together with the encouraging cross-site behaviour, suggest that multimodal Transformers could support early detection of anomalous ground motion and prioritisation of areas for further inspection or higher-frequency acquisitions.

Several avenues remain for future research. First, the present analysis focuses on single-step forecasting at a fixed temporal resolution; extending the framework to multi-step horizons, irregular acquisition intervals and real-time updating will be important to assess robustness under more realistic conditions. Second, incorporating additional covariates such as topography, land cover, groundwater levels or anthropogenic loading indicators could further enhance predictive skill and help disentangle different physical drivers of deformation. Third, combining the proposed multimodal Transformer with uncertainty quantification and interpretability techniques (e.g. ensemble methods, quantile regression, SHAP analysis or attention visualisation) may help bridge the gap between purely data-driven forecasts and process-based understanding of land deformation, thereby increasing the trustworthiness and uptake of deep learning models in geohazard assessment and infrastructure management.

Declaration of generative AI and AI-assisted technologies in the manuscript preparation process

During the preparation of this work the author(s) used ChatGPT (OpenAI) and other large language model-based assistants in order to improve the clarity and readability of the text, to refine figure captions and schematic descriptions, and to obtain suggestions for code structuring and response wording. After

using these tools, the author(s) reviewed and edited all generated content as needed and take full responsibility for the content of the published article.

Acknowledgment

This research was conducted with the financial support of Science Foundation Ireland under Grant Agreement No. 13/RC/2106_P2 at the ADAPT SFI Research Centre at University College Dublin. ADAPT, the SFI Research Centre for AI-Driven Digital Content Technology is funded by Science Foundation Ireland through the SFI Research Centres Programme. This work is partly supported by China Scholarship Council (202306540013).

References

- [1] T. Q. Cuong, D. H. Tong Minh, L. Van Trung, T. Le Toan, Ground subsidence monitoring in vietnam by multi-temporal insar technique, in: 2015 IEEE International Geoscience and Remote Sensing Symposium (IGARSS), 2015, pp. 3540–3543. doi:10.1109/IGARSS.2015.7326585.
- [2] D. Tapete, F. Cigna, R. Lasaponara, N. Masini, P. Milillo, Deformation analysis of a metropolis from c- to x-band psi: Proof-of-concept with cosmo-skymed over rome, italy, in: 2015 IEEE International Geoscience and Remote Sensing Symposium (IGARSS), 2015, pp. 4606–4609. doi:10.1109/IGARSS.2015.7326854.
- [3] F. Zhao, J. J. Mallorqui, J. M. Lopez-Sanchez, Impact of sar image resolution on polarimetric persistent scatterer interferometry with amplitude dispersion optimization, IEEE Transactions on Geoscience and Remote Sensing 60 (2022) 1–10. doi:10.1109/TGRS.2021.3059247.
- [4] S. Azadnejad, A. Hryszewicz, A. Trafford, F. O'Loughlin, E. Holohan, F. Kelly, S. Donohue, Insar supported by geophysical and geotechnical information constrains two-dimensional motion of a railway embankment constructed on peat, Engineering Geology 333 (2024) 107493. doi:https://doi.org/10.1016/j.enggeo.2024.107493. URL <https://www.sciencedirect.com/science/article/pii/S0013795224000917>
- [5] B. Osmanoglu, F. Sunar, S. Wdowinski, E. Cabral-Cano, Time series analysis of insar data: Methods and trends, ISPRS Journal of Photogrammetry and Remote Sensing 115 (2016) 90–102, theme issue 'State-of-the-art in photogrammetry, remote sensing and spatial information science'. doi:https://doi.org/10.1016/j.isprsjprs.2015.10.003. URL <https://www.sciencedirect.com/science/article/pii/S0924271615002269>

[6] Y. Yan, G. Mauris, E. Trouve, V. Pinel, Fuzzy uncertainty representations of coseismic displacement measurements issued from sar imagery, *IEEE Transactions on Instrumentation and Measurement* 61 (5) (2012) 1278–1286. doi:10.1109/TIM.2011.2175825.

[7] J. S. Park, C. K. Kim, S. O. Park, A stretched deramping radar technique for high-resolution sar processing in ka-band using the extended integration time, *IEEE Transactions on Instrumentation and Measurement* 72 (2023) 1–11. doi:10.1109/TIM.2023.3264048.

[8] R. Palamà, M. Cuevas-González, A. Barra, Q. Gao, S. Shahbazi, J. A. Navarro, O. Monserrat, M. Crosetto, Automatic ground deformation detection from european ground motion service products, in: *IGARSS 2023 - 2023 IEEE International Geoscience and Remote Sensing Symposium*, 2023, pp. 8190–8193. doi:10.1109/IGARSS52108.2023.10281998.

[9] M. Costantini, F. Minati, F. Trillo, A. Ferretti, F. Novali, E. Passera, J. Dehls, Y. Larsen, P. Marinkovic, M. Eineder, R. Brcic, R. Siegmund, P. Kotzerke, M. Probeck, A. Kenyeres, S. Proietti, L. Solari, H. S. Andersen, European ground motion service (egms), in: *2021 IEEE International Geoscience and Remote Sensing Symposium (IGARSS)*, 2021, pp. 3293–3296. doi:10.1109/IGARSS47720.2021.9553562.

[10] M. Crosetto, B. Crippa, M. Mróz, M. Cuevas-González, S. Shahbazi, Applications based on egms products: A review, *Remote Sensing Applications: Society and Environment* 37 (2025) 101452. doi:<https://doi.org/10.1016/j.rsase.2025.101452>. URL <https://www.sciencedirect.com/science/article/pii/S2352938525000059>

[11] S. Azadnejad, Y. Maghsoudi, D. Perissin, Evaluation of polarimetric capabilities of dual polarized sentinel-1 and terrasar-x data to improve the psinsar algorithm using amplitude dispersion index optimization, *International Journal of Applied Earth Observation and Geoinformation* 84 (2020) 101950. doi:<https://doi.org/10.1016/j.jag.2019.101950>. URL <https://www.sciencedirect.com/science/article/pii/S0303243419302995>

[12] J. Rivera-Rivera, M. Béjar-Pizarro, H. Aguilera, C. Guardiola-Albert, C. Husillos, P. Ezquerro, A. Barra, R. M. Mateos, M. Cuevas-González, R. Sarro, O. Monserrat, M. Martínez-Corbella, M. Crosetto, J. López-Vinielles, Automatic classification of active deformation areas based on synthetic aperture radar data and environmental covariates using machine learning—application in se spain, *Environmental Sciences Proceedings* 28 (1) (2023). doi:10.3390/environsciproc2023028015. URL <https://www.mdpi.com/2673-4931/28/1/15>

[13] R. S. Kuzu, L. Bagaglini, Y. Wang, C. O. Dumitru, N. A. A. Braham, G. Pasquali, F. Santarelli, F. Trillo, S. Saha, X. X. Zhu, Automatic detection of building displacements through unsupervised learning from insar data, *IEEE Journal of Selected Topics in Applied Earth Observations and Remote Sensing* 16 (2023) 6931–6947. doi:10.1109/JSTARS.2023.3297267.

[14] B. Yu, H. Yin, Z. Zhu, Spatio-temporal graph convolutional networks: A deep learning framework for traffic forecasting, *arXiv preprint arXiv:1709.04875* (2017).

[15] W. Yao, S. Azadnejad, B. Huang, S. Donohue, S. Dev, A deep learning approach for spatio-temporal forecasting of insar ground deformation in eastern ireland (2025). *arXiv:2509.18176* URL <https://arxiv.org/abs/2509.18176>

[16] W. Yao, B. Huang, S. Dev, Multi-modal spatio-temporal transformer for high-resolution land subsidence prediction (2025). *arXiv:2509.25393* URL <https://arxiv.org/abs/2509.25393>

[17] X. Shi, Z. Chen, H. Wang, D. Yeung, W. Wong, W. Woo, Convolutional LSTM network: A machine learning approach for precipitation nowcasting, *CoRR abs/1506.04214* (2015). *arXiv:1506.04214* URL <http://arxiv.org/abs/1506.04214>

[18] A. Vaswani, N. Shazeer, N. Parmar, J. Uszkoreit, L. Jones, A. N. Gomez, L. Kaiser, I. Polosukhin, Attention is all you need, *CoRR abs/1706.03762* (2017). *arXiv:1706.03762* URL <http://arxiv.org/abs/1706.03762>